Applied Catalysis B: Environmental 233 (2018) 26–34

Contents lists available at ScienceDirect

Applied Catalysis B: Environmental

journal homepage: www.elsevier.com/locate/apcatb

Construction of network-like and flower-like 2H-$MoSe_2$ nanostructures coupled with porous g-C_3N_4 for noble-metal-free photocatalytic H_2 evolution under visible light

Deqian Zeng[a,b], Pengyuan Wu[a], Wee-Jun Ong[b,*], Baoshan Tang[c], Mingda Wu[d], Hongfei Zheng[a], Yuanzhi Chen[a,*], Dong-Liang Peng[a,*]

[a] *Department of Materials Science and Engineering, Collaborative Innovation Center of Chemistry for Energy Materials, College of Materials, Xiamen University, Xiamen 361005, China*

[b] *Institute of Materials Research and Engineering (IMRE), Agency for Science, Technology and Research (A*STAR), 2 Fusionopolis Way, Innovis, Singapore 138634, Singapore*

[c] *Department of Materials Science and Engineering, National University of Singapore, Singapore 117576, Singapore*

[d] *School of Materials Science and Engineering, Nanyang Technological University, 50 Nanyang Avenue, Singapore 639798, Singapore*

ARTICLE INFO

Keywords:
Graphitic carbon nitride
Layered materials
Molybdenum diselenide
Noble-metal-free
Photocatalytic hydrogen evolution

ABSTRACT

Colloidally synthesized flower-like and network-like $MoSe_2$ nanostructures are coupled with porous g-C_3N_4 nanosheets through a facile solution-phase route. Herein, two distinct morphological structures of $MoSe_2$/g-C_3N_4 hybrid nanocomposites are applied as noble-metal-free photocatalysts for hydrogen (H_2) evolution. In the resulting optimally-designed hybrid systems, the optimal flower-like and network-like $MoSe_2$ nanostructures loading is determined to be 5 wt%, attaining a maximum H_2 evolution rate of 114.5 μmol h^{-1} g^{-1} and 136.8 μmol h^{-1} g^{-1}, respectively. In comparison with flower-like $MoSe_2$ cocatalysts, the network-like $MoSe_2$ hybridized with g-C_3N_4 endows excellent photocatalytic H_2 evolution activity. This phenomenon stems from the intimate formation of unique sheet-on-sheet nanoarchitecture, which is auspicious for the absorption of light and high-efficiency separation of photoexcited electron-hole pairs to hamper the charge recombination. The present studies elucidate the prevailing role of $MoSe_2$ nanostructures as active catalytic sites for H_2 evolution, and importantly, the hybrid systems exhibit high photocatalytic stability. Collectively, the work opens up new insights for the utilization of low-cost $MoSe_2$ nanomaterials as remarkable noble-metal-free cocatalysts for effective photocatalytic H_2 generation.

1. Introduction

Photocatalytic hydrogen (H_2) evolution using semiconductor photocatalysts is profiled as one of the most budding strategies to combat the imminent energy crisis and increasingly aggravated environmental issues [1]. In recent years, graphitic carbon nitride (g-C_3N_4) has triggered a blossoming interest in the field of water splitting owing to its visible-light-responsiveness, low cost, facile preparation, environmentally benign, and high chemical- and photo-stability [2–6]. However, the photocatalytic H_2 production activity of pristine g-C_3N_4 is thwarted by its high recombination rate of photogenerated charge carriers [7–12]. Therefore, the presence of co-catalysts is devoted to serving as electron sinks and shuttling the photoexcited electrons, as well as to provide exceptional proton reduction reaction active sites for H_2 evolution [13,14]. In order to avoid the use of high cost and scarcity of Pt cocatalyst, a great deal of incessant efforts has been dedicated to constructing cost-effective and high efficiency of g-C_3N_4-based systems with the incorporation of noble-metal-free cocatalysts [3,7,14]. To date, transition metal sulfides such as MoS_2 [15,16], NiS [17,18], and WS_2 [19,20] are coupled with g-C_3N_4 for the efficient photocatalytic H_2 production. Additionally, transition metal phosphides, namely Ni_2P [21–24], $Ni_{12}P_5$ [25,26], NiCoP [27,28], Fe_xP [29], and CoP [30–32], which function as remarkable reduction cocatalysts modified g-C_3N_4, are propitious to accelerate the charge transfer and separation, resulting in the enhanced photocatalytic H_2 evolution. However, in comparison to metal sulfides and metal phosphides, transition metal selenides are relatively seldom discussed in the literature at present, especially for the $MoSe_2$ nanostructures, thus dictating a necessity for further exploration in the near future.

Up to now, molybdenum-based compounds, including MoS_2

* Corresponding authors.
E-mail addresses: ongweejun@gmail.com (W.-J. Ong), yuanzhi@xmu.edu.cn (Y. Chen), dlpeng@xmu.edu.cn (D.-L. Peng).

https://doi.org/10.1016/j.apcatb.2018.03.102
Received 15 November 2017; Received in revised form 12 February 2018; Accepted 26 March 2018
Available online 27 March 2018

[33,34], Mo_2C [35,36], and $MoSe_2$ [37–40] have been found to demonstrate high electrochemical catalytic activity and long-term stability for the hydrogen evolution reaction (HER) process. Furthermore, MoS_2 has been widely used as an indispensable non-noble-metal cocatalyst for the modification of semiconductor photocatalysts toward sustainable H_2 evolution [41–47]. For example, MoS_2 quantum dots can act as highly-efficient cocatalysts when coupled with CdS for boosting the photocatalytic H_2 evolution activity [47]. Compared to the general MoS_2 nanostructure, $MoSe_2$ has a layered structure and exhibits more metallic in nature, which markedly provides higher electrical conductivity, hence favoring the electrochemical reactions [48,49]. Such intriguing characteristics render a magnificent prospect of $MoSe_2$ to act as a compelling candidate for photocatalysis and many other energy applications. To the best of our knowledge, only a few recent reports focus on the $MoSe_2$ cocatalysts for boosted photocatalytic H_2 evolution [50,51]. In our very recent investigation, the functional roles of $MoSe_2$ serve as a superior electron storage site and a H_2-evolution reaction catalyst for ameliorated photocatalytic H_2 evolution in the $ZnIn_2S_4$/$MoSe_2$ hierarchical sheet-on-sheet system [51]. Therefore, it is of sustained interest to integrate layered $MoSe_2$ and 2D sheet-like porous g-C_3N_4, which are worthy of note for examining their optical and catalytic activity.

Hitherto, extensive studies have exemplified that the size, phase, shape and morphology of a catalyst nanostructure profoundly affect the catalytic performance [52,53]. For example, the crystalline phase of nickel phosphide is essential for influencing the electrocatalytic properties [54]. Moreover, different morphological designs on engineering the heterojunction interface between two nanomaterials play a substantial effect on the photocatalytic activity. Bera and co-workers reported that 2D-2D CdS nanosheets/reduced graphene oxide (RGO) composites were more effective to harvest photons from solar light and transport electrons to reactive sites with respect to 0D-2D CdS nanoparticles/RGO and 1D-2D CdS nanorod/RGO composite samples [55]. According to our previous report, the structure and morphology variations impart significant influences on the HER activity of $MoSe_2$ nanostructures [40]. In view of that, it is conspicuous that dissimilar morphologies and nanostructures of $MoSe_2$ cocatalysts would give rise to considerable effects on the photocatalytic performance of the hybrid systems. Essentially, the synthesis of highly efficient $MoSe_2$/g-C_3N_4 hybrids for the photocatalytic H_2 evolution under visible light is imperative to uncover the functionality of transition metal selenide cocatalysts in the nanocomposites.

Herein, the colloidally synthesized flower-like and network-like $MoSe_2$ are successfully coupled with porous g-C_3N_4 nanosheets by means of a simple general solution-phase approach. The composition, properties and photocatalytic performance of the $MoSe_2$/g-C_3N_4 hybrid systems are systematically studied. Fascinatingly, these two typical $MoSe_2$/g-C_3N_4 hybrid photocatalysts present superior H_2 evolution under visible light radiation without any assistance of noble metals. It is apparent that more efficient catalytic performance is observed in the g-C_3N_4-based hybrid system by loading with network-like $MoSe_2$.

2. Experimental

2.1. Catalyst synthesis

Preparation of $MoSe_2$ nanostructures: The flower-like and network-like $MoSe_2$ were prepared *via* a facile solution-phase technique based on our previous report [40]. Briefly, for the synthesis of flower-like $MoSe_2$, 0.6 mmol of molybdenum hexacarbonyl ($Mo(CO)_6$) and 10 mL of oleic acid (OA) were placed in a 100 mL of round-bottom flask. The mixture was maintained at 85 °C for 5 min to dissolve the precursor, and subsequently heated up to 200 °C. Next, 8 mL of the prepared selenide-1-octadecene (Se-ODE) solution (0.15 mol/L) was injected into the mixture through a syringe pump at a speed of 0.4 mL/min, and then the mixture was further kept at 200 °C for 30 min. After that, the mixture was heated up to 300 °C and kept for 30 min before cooling down to room temperature naturally. Finally, the final black products were collected by centrifugation and washed with a mixture of hexane and ethanol for several times before drying in vacuum. For the preparation of network-like $MoSe_2$, 5 mL of OA and 5 mL of oleylamine (OAm) were used to replace 10 mL of OA, and other subsequent steps were identical to the synthesis of flower-like $MoSe_2$ nanostructure.

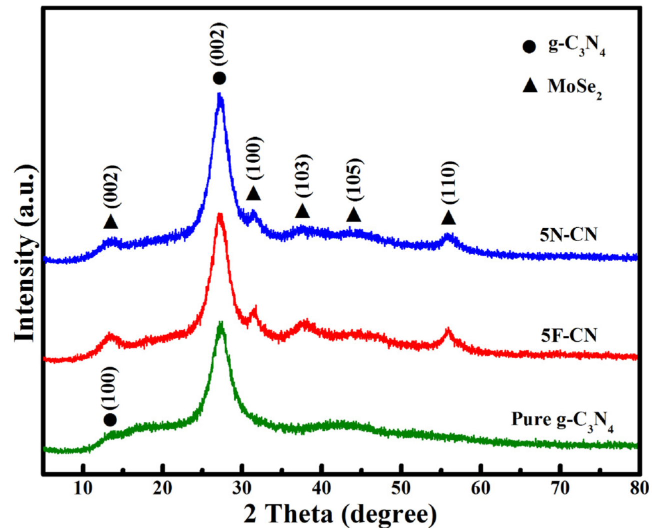

Fig. 1. XRD patterns of pure g-C_3N_4, 5F-CN and 5N-CN samples.

Preparation of $MoSe_2$/g-C_3N_4 heterojunction nanostructures: Firstly, porous g-C_3N_4 was synthesized by the thermal polycondensation of urea, which has been reported in our previous work [56]. The colloidally synthesized flower-like and network-like $MoSe_2$ nanostructures were incorporated into the porous g-C_3N_4 nanosheets through a simple solution-phase method based on our recent report [22,25]. In short, 300 mg of g-C_3N_4 and a varied amount of flower-like or network-like $MoSe_2$ were ultrasonicated in the mixture of DMF/hexane/ethanol for 60 min. The products were washed with ethanol by centrifugation twice followed by suspending the products in ethanol/hexane solution and performing ultrasonication for additional 60 min. The resulting precipitate was separated by centrifugation and washed with ethanol before it was dried in a vacuum oven at 120 °C for 6 h.

2.2. Characterization

Transmission electron microscopy (TEM) images, energy dispersive X-ray (EDX) spectroscopy and TEM-EDX elemental mapping were obtained with a TECNAI F-30 transmission electron microscope operating at 300 kV. Powder X-ray diffraction (XRD) data were performed on a Bruker D8 Advance X-ray powder diffractometer with Cu Kα radiation. Ultraviolet-visible (UV–vis) absorption spectra were collected by using a Cary 5000 UV–vis spectrometer. Nitrogen adsorption-desorption isotherms, Brunauer-Emmett-Teller (BET) surface area and pore-size distribution were obtained on a Micromeritics ASAP 2020 adsorption apparatus with the samples degassed at 160 °C for 6 h prior to measurements. The photoluminescence (PL) spectra were acquired on a FLS980 spectrophotometer (Edinburgh Instrument). Time-resolved photoluminescence (TRPL) measurements were conducted by using a time-correlated single photon counting system (PicoHarp 300, PicoQuant) at an excitation wavelength of 405 nm. Fourier transform infrared (FTIR) spectra were recorded with a Nicolet Nexus-670 FTIR spectrometer. X-ray photoelectron spectroscopy (XPS) measurements were carried out on a VG ESCALAB 220i-XL system.

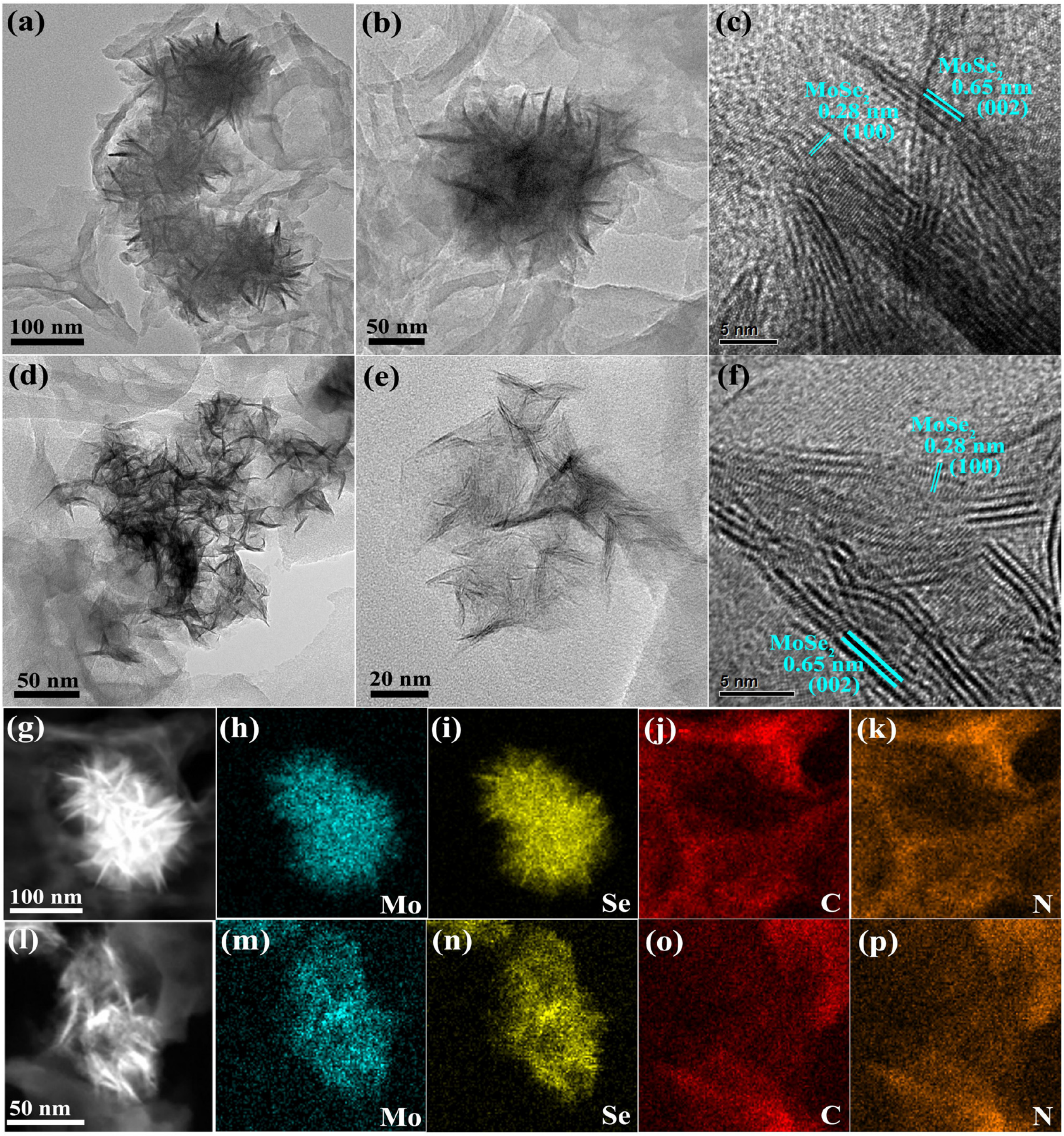

Fig. 2. (a), (d) Low-magnification, (b), (e) high-magnification TEM images, and (c), (f) HRTEM images of 5F-CN and 5N-CN, respectively. (g), (l) HAADF images, (h)–(k) and (m)–(p) the corresponding STEM elemental mapping of Mo, Se, C and N of 5F-CN and 5N-CN, respectively.

2.3. Photocatalytic activity test

The photocatalytic H_2 production reactions were performed in a closed and connected vacuum circulatory system using a 250 mL of Pyrex flask at room temperature. The as-prepared $MoSe_2$/g-C_3N_4 photocatalyst (60 mg) was uniformly dispersed by ultrasonication in 150 mL of aqueous solution containing 10 vol% triethanolamine (TEOA) as the sacrificial reagent. The reactant mixture was degassed by evacuating the reactor followed by purging with argon. Next, a circular cooling water system was turned on and the reactor was vertically irradiated by a 300 W high-pressure Xe lamp (CEL-HXUV300, Beijing Aulight Co., Ltd.) coupled with a UV-cutoff filter ($\lambda > 420$ nm) under magnetic stirring. The amount of H_2 evolved was analyzed using a gas chromatography (GC) system (Shimadzu GC-2014, Ar as the carrier gas, a 5 Å molecular sieve column, a thermal conductivity detector (TCD)). Cycling tests of photocatalytic H_2 production were conducted by evacuating under vacuum and purging the suspension with argon gas for 50 min to completely remove the H_2 produced in the previous cycle without changing the original solution.

2.4. Photoelectrochemical (PEC) measurements

Photoelectrochemical (PEC) analysis was performed on a VSP-300 (Biologic) potentiostat *via* a typical three-electrode configuration under visible light irradiation. The working electrodes were prepared based on our previous report [22]. 6 mg of photocatalyst powder was added

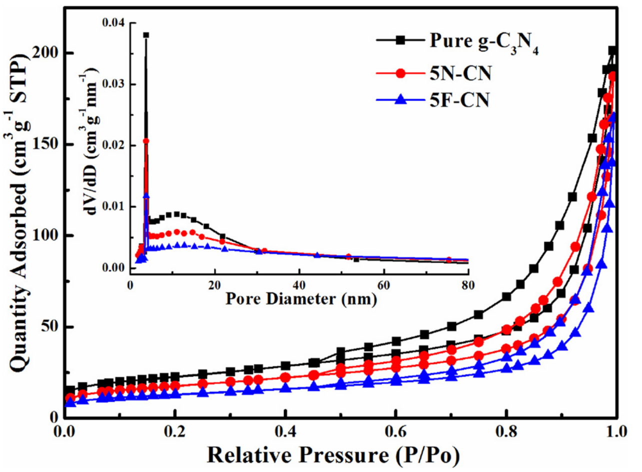

Fig. 3. N_2 adsorption-desorption isotherms and the corresponding pore-size distribution curves (inset) of the as-prepared g-C_3N_4, 5F-CN and 5N-CN samples.

into 3 mL of ethanol and the dispersion was sonicated for 10 min. The prepared slurry was coated onto a 1 cm × 2 cm carbon fiber paper. After that, the carbon fiber paper was dried in a vacuum oven at 120 °C for 3 h to improve the adhesion of the sample onto the carbon fiber substrate. In the PEC system, a saturated Ag/AgCl electrode and a piece of Pt sheet acted as the reference and counter electrodes, respectively. Meanwhile, 0.1 M of Na_2SO_4 aqueous solution was employed as the electrolyte. The transient photocurrent response results were recorded with the lamp on-off cycle under an applied potential of 0.5 V. Electrochemical impedance spectroscopy (EIS) spectra were obtained over a frequency range of 10^{-1} to 10^5 Hz at an applied bias of 0.5 V *vs.* Ag/AgCl with an alternating current perturbation signal of 0.01 V in the dark and under visible light.

3. Results and discussion

Two different morphological structures of $MoSe_2$ nanostructures are coupled with g-C_3N_4 nanosheets through a facile solution-phase method. At the first stage, mixing two immiscible solutions ($MoSe_2$ in hexane and g-C_3N_4 in DMF) via sonication was an essential step to deposit $MoSe_2$ on 2D g-C_3N_4, in which g-C_3N_4 transferred to the upper hexane solution and $MoSe_2$ could be facilely adsorbed on the surface of g-C_3N_4 due to the adsorption effect of functional groups on g-C_3N_4 [22,25]. Ethanol was added for the formation of homogeneous solution, which can be attributed to the fact that ethanol/hexane or ethanol/DMF mixtures are miscible solutions. At the second stage, after washing with ethanol, the products were sonicated in ethanol/hexane solution to achieve more intimate contact between $MoSe_2$ and g-C_3N_4, and the low boiling point solvents such as ethanol/hexane can be easily removed upon drying in vacuum. Herein, the hybrid samples comprising flower-like and network-like $MoSe_2$ are denoted as F-CN and N-CN, respectively. Based on different weight loadings (x wt%) of flower-like and network-like $MoSe_2$ nanostructures in the $MoSe_2$/g-C_3N_4 system,

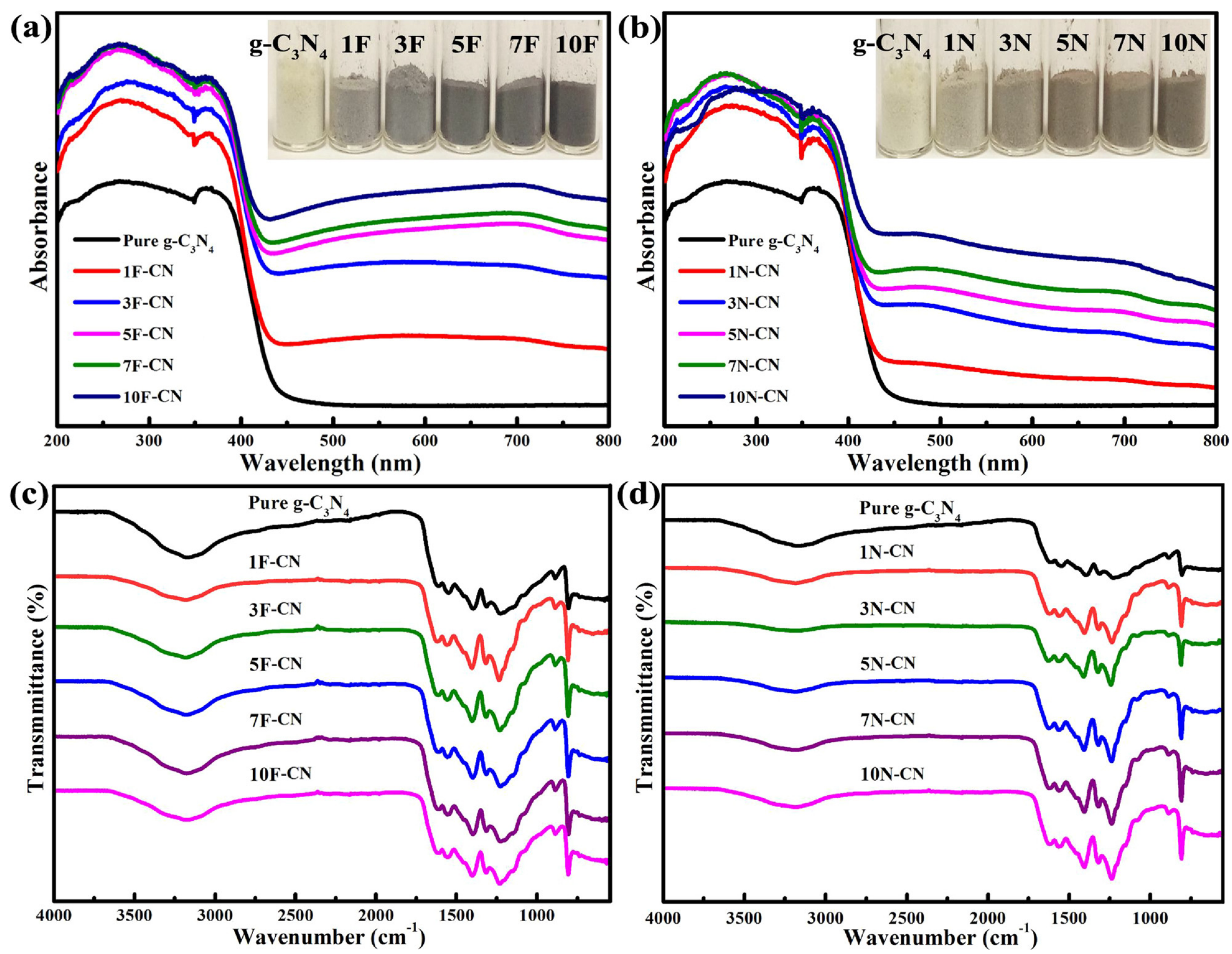

Fig. 4. UV–vis diffuse reflectance spectra of pure g-C_3N_4, F-CN (a) and N-CN (b) samples with different $MoSe_2$ contents. Insets in (a) and (b) present the digital photographs of the studied samples. FTIR spectra of pure g-C_3N_4, F-CN (c) and N-CN (d) samples with different $MoSe_2$ contents.

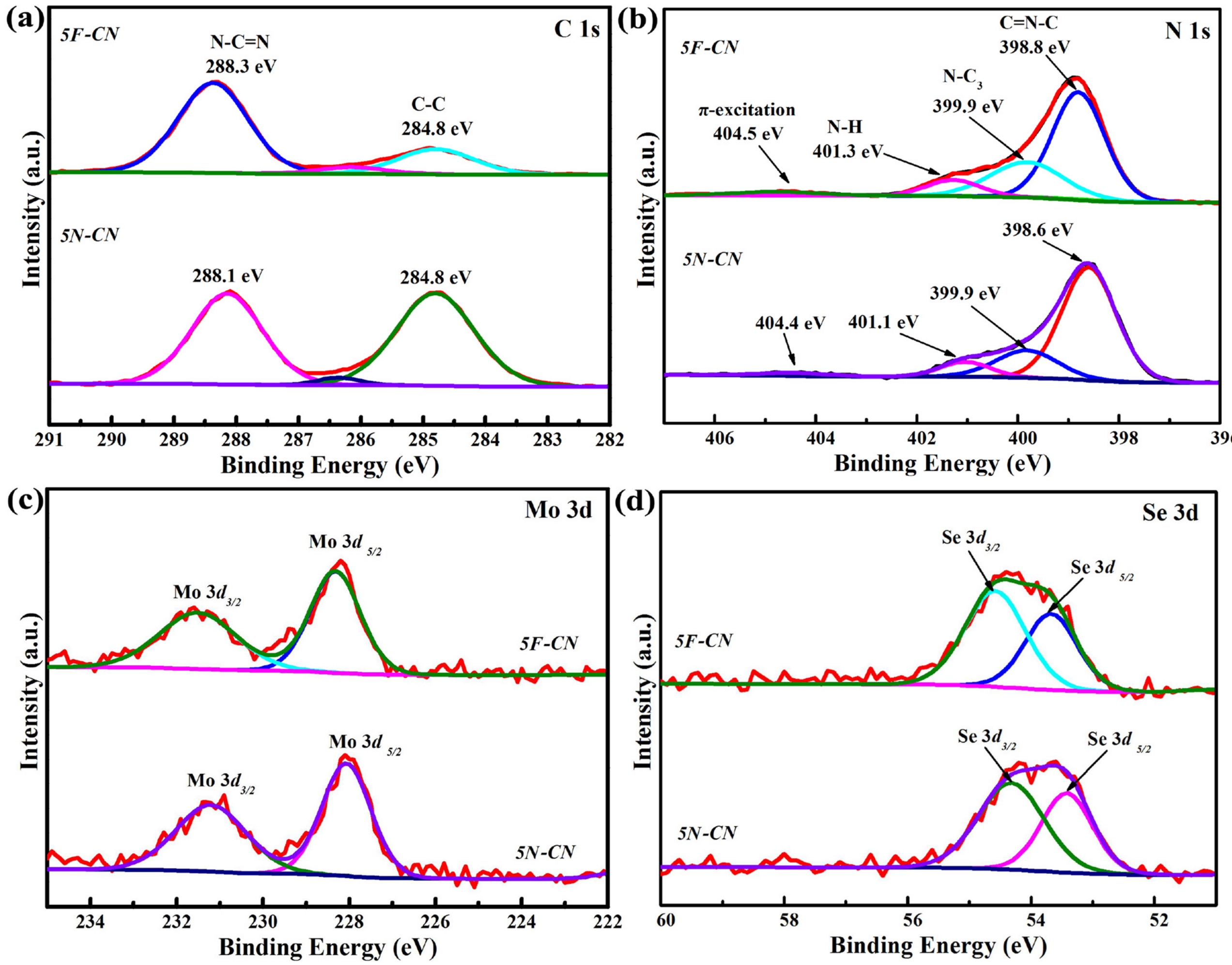

Fig. 5. High resolution XPS spectra of (a) C 1s, (b) N 1s, (c) Mo 3d and (d) Se 3d of the 5F-CN and 5N-CN samples.

the hybrid photocatalysts are represented as *x*F-CN and *x*N-CN. For example, 5F-CN and 5N-CN refer to $g-C_3N_4$-based hybrid system consisting of 5 wt% of flower-like $MoSe_2$ and network-like $MoSe_2$, respectively.

The crystal structure of the samples was investigated using XRD. Fig. 1 illustrates the XRD patterns of pure $g-C_3N_4$, 5F-CN and 5N-CN samples. It can be noticeably seen that pure $g-C_3N_4$ has two characteristic peaks appeared at 13.0° and 27.4°, corresponding to the (100) plane with in-plane structural packing and (002) plane of interlayer stacking with conjugated aromatic systems, respectively. Such diffraction peaks are consistent with the widely reported $g-C_3N_4$ [57]. For the hybrid samples, an apparent diffraction peak located at 27.4°, belonging to $g-C_3N_4$, is shown in both 5F-CN and 5N-CN samples. In addition to that, other diffraction peaks in the heterostructure samples can be clearly indexed to 2H-$MoSe_2$ (JCPDS#29-0914) [40], and also the (100) diffraction peak of $g-C_3N_4$ with low intensity is overlapped by the (002) diffraction peak of $MoSe_2$, corroborating the successful formation of a $MoSe_2$ and $g-C_3N_4$ nanocomposite. Furthermore, the intensities of diffraction peaks of $MoSe_2$ gradually enhance with an increase in the contents of $MoSe_2$ present in the $MoSe_2$/$g-C_3N_4$ heterojunction samples with desirable architectural morphologies (Fig. S1 and Fig. S2).

The structure and morphology of pure $g-C_3N_4$, flower-like and network-like $MoSe_2$ and the representative $MoSe_2$/$g-C_3N_4$ hybrid samples were studied using TEM. As shown in Fig. S3, the TEM image of pure $g-C_3N_4$ presents its typical nanosheet and porous structures. Fig. S4 depicts the TEM images of flower-like and network-like $MoSe_2$. Interestingly, the flower-like $MoSe_2$ nanostructure is assembled by multiple nanosheets with a total size in the range of 100–200 nm (Fig. S4a), whereas the network-like $MoSe_2$ nanostructure is composed of ultrathin nanosheets which orient to different directions and eventually it becomes more porous (Fig. S4b). These findings are in accordance with our previous report [40]. The TEM images of the $MoSe_2$/$g-C_3N_4$ sample are delineated in Fig. 2. As shown in Fig. 2a–b, the flower-like $MoSe_2$ is loaded on the $g-C_3N_4$ nanosheets with intimate interaction between $MoSe_2$ and $g-C_3N_4$ nanosheets. The HRTEM image (Fig. 2c) of the 5F-CN sample demonstrates a clear lattice fringe with the spacing of 0.65 nm and 0.28 nm, corresponding to the (002) and (100) planes of 2H-$MoSe_2$, respectively. On the other hand, the TEM images (Fig. 2d–e) of network-like $MoSe_2$ confirm the hybridization of $MoSe_2$ and $g-C_3N_4$ nanosheets, in which the ultrathin nanosheets of network-like $MoSe_2$ are decorated on $g-C_3N_4$ nanosheets. The HRTEM image (Fig. 2f) of the 5N-CN sample ascertains the lattice fringes of $MoSe_2$, which are in consensus with the (002) and (100) planes of 2H-$MoSe_2$. The high-angle annular dark field (HAADF) image and the corresponding scanning TEM (STEM) elemental mapping images of 5F-CN and 5N-CN are presented in Fig. 2g–k and Fig. 2l–p, respectively. It is evident that a homogeneous distribution of C and N elements is observed over the two typical hybrid samples, while the Mo and Se elements only exist in the flower-like and network-like $MoSe_2$ nanostructures which are deposited on the $g-C_3N_4$ matrix. The EDX spectra (Fig. S5) of 5F-CN and 5N-CN further prove the presence of Mo, Se, C and N elements in both $MoSe_2$/$g-C_3N_4$ hybrid systems.

The nitrogen adsorption-desorption isotherms and the corresponding pore size distribution curves of pure $g-C_3N_4$, 5F-CN and 5N-

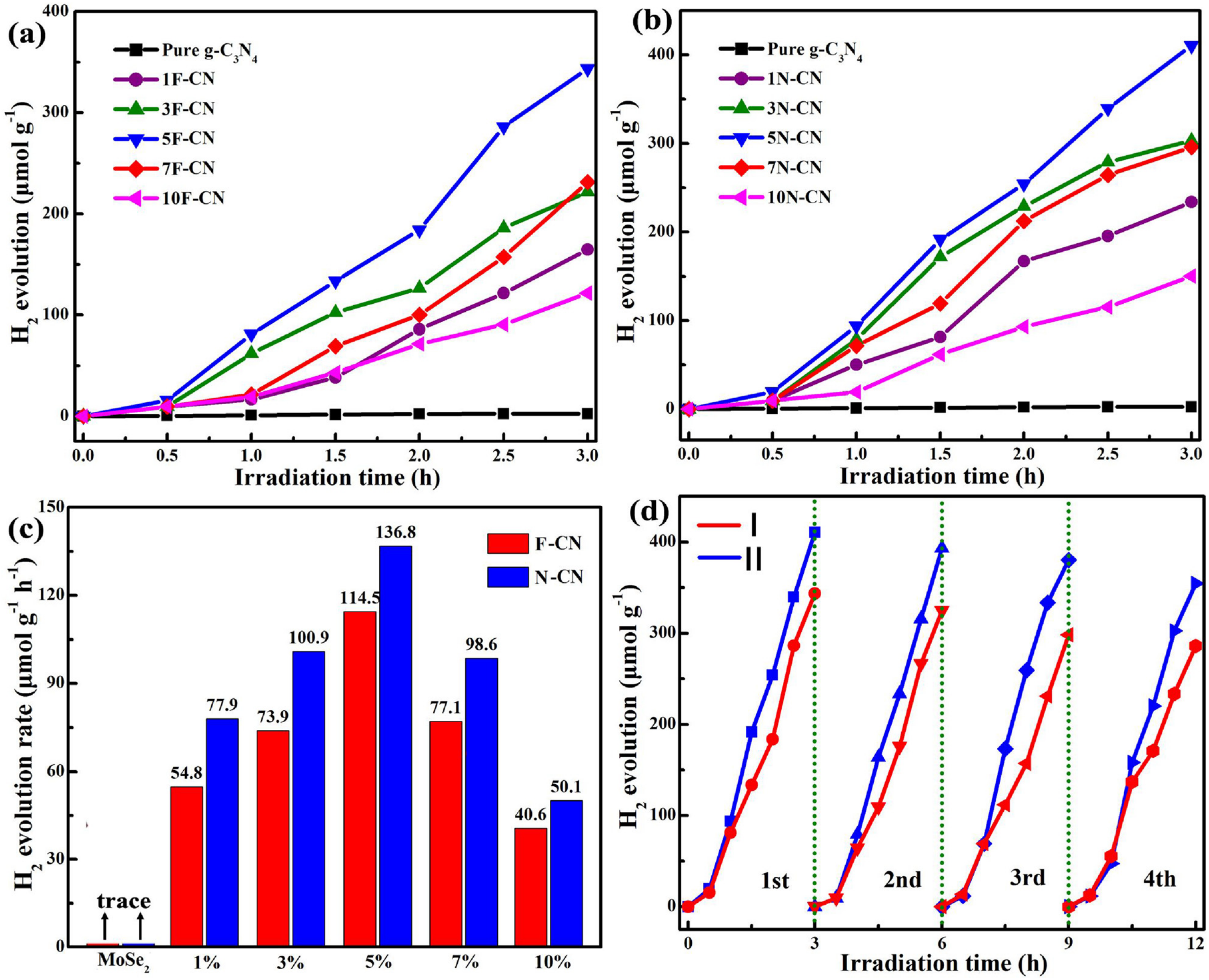

Fig. 6. Time courses of photocatalytic H_2 evolution over pure g-C_3N_4, F-CN (a) and N-CN (b). (c) Comparison of average photocatalytic H_2 evolution rates of the pristine $MoSe_2$, 5F-CN and 5N-CN samples. (d) Recycle runs of H_2 evolution over the (I) 5F-CN and (II) 5N-CN.

CN are displayed in Fig. 3. It can be seen that pure g-C_3N_4, 5F-CN and 5N-CN have type IV isotherms and type H3 hysteresis loops, indicating the mesoporous structure in pure g-C_3N_4 and both hybrid samples. Among these studied samples, pure g-C_3N_4 shows the highest BET specific surface area of 79.6 $m^2\,g^{-1}$, whereas 5N-CN and 5F-CN have specific surface areas of 62.2 and 45.3 $m^2\,g^{-1}$, respectively. The decrease of surface area in the hybrid samples can be accredited to the deposition of $MoSe_2$ nanostructures on the surface of g-C_3N_4. Importantly, the BET surface area and total pore volume of 5N-CN (62.2 $m^2\,g^{-1}$ and 0.23 $cm^3\,g^{-1}$) are higher than those of 5F-CN (45.3 $m^2\,g^{-1}$ and 0.18 $cm^3\,g^{-1}$) by using the same weight percent of $MoSe_2$ loaded onto g-C_3N_4. As such, this phenomenon can be originated from the higher surface area of network-like $MoSe_2$ nanostructures as reported in our previous finding [40].

Fig. 4a and b display the UV–vis diffuse reflectance spectra of pure g-C_3N_4, F-CN and N-CN samples with different $MoSe_2$ contents. It is noted that pure g-C_3N_4 and both types of $MoSe_2$/g-C_3N_4 hybrid photocatalysts feature an absorption edge at around 455 nm, corresponding to a band gap of *ca.* 2.73 eV, inferring that the $MoSe_2$/g-C_3N_4 samples retain the intrinsic band gap of g-C_3N_4 even after loading with flower-like or network-like $MoSe_2$. In contrast to pure g-C_3N_4, the $MoSe_2$/g-C_3N_4 hybrid photocatalysts unveil significantly enhanced intensity in absorbance at wavelengths above 420 nm with increasing the amounts of $MoSe_2$ nanostructures. This can be substantiated by the color change from light yellow to deep color with increasing $MoSe_2$ contents in the hybrid systems (insets in Fig. 4a and b). Fig. 4c and d manifest the FTIR spectra of pure g-C_3N_4, a series of F-CN and N-CN samples. All the $MoSe_2$/g-C_3N_4 samples possess similar characteristic features to the bare g-C_3N_4. The broad absorption band located in the range of 3100–3300 cm^{-1} is ascribed to the stretching modes of secondary and primary amines and their intermolecular hydrogen-bonding interactions [58]. Several strong bands in the 1200–1650 cm^{-1} region are assigned to the typical stretching modes of C—N heterocycles [59], whereas the absorption band situated at 810 cm^{-1} is originated from the characteristic breathing mode of CN heterocycles of triazine units [60]. The FTIR results imply that there is no noticeable variation in the stretching and bending vibrations of g-C_3N_4 after hybridizing with flower-like and network-like $MoSe_2$.

The surface chemical states of 5F-CN and 5N-CN were examined by XPS. As depicted in Fig. 5a and b, the C 1s and N 1s XPS spectra exemplify the characteristic nature of g-C_3N_4 [26]. The high resolution XPS spectra of O 1s (Fig. S6) are characterized to the surface adsorbed oxygen species (533.1 eV) and C—O bonds (531.6 eV) [21]. As illustrated in Fig. 5c, the Mo $3d_{3/2}$ and $3d_{5/2}$ peaks are positioned close to 231.5 and 228.3 eV for 5F-CN, and 231.2 and 228.1 eV for 5N-CN, which is accredited to the Mo^{4+} valence state [50]. The Se 3d XPS spectra (Fig. 5d) indicate that the Se $3d_{3/2}$ and $3d_{5/2}$ peaks are located at 54.6 and 53.7 eV for 5F-CN, and 54.3 and 53.4 eV for 5N-CN, corresponding to Se^{2-}. Notably, the obtained Mo 3d and Se 3d XPS spectra are in agreement with the $MoSe_2$ system, further elucidating the

successful hybridization of $MoSe_2$ in the g-C_3N_4 hybrid photocatalysts.

The photocatalytic H_2 evolution activity over pure g-C_3N_4 and two typical types of $MoSe_2$/g-C_3N_4 hybrid systems were evaluated under visible light irradiation (λ > 420 nm) in the absence of noble metals. The time courses of photocatalytic H_2 generation over pure g-C_3N_4, F-CN and N-CN are displayed in Fig. 6a and b. For pure g-C_3N_4, the photocatalytic rate of H_2 generation is negligible due to the rapid recombination of photo-excited electron-hole pairs. After incorporating a small amount of $MoSe_2$ nanostructures into g-C_3N_4, the $MoSe_2$/g-C_3N_4 hybrid samples can conspicuously ameliorate the H_2 evolution activity. Among all studied samples, the optimal photocatalytic activity is achieved at 5F-CN and 5N-CN samples loading with 5 wt% of flower-like and network-like $MoSe_2$ content in the F-CN and N-CN heterostructure systems, respectively. Moreover, a detailed comparison of the average photocatalytic H_2 evolution is delineated in Fig. 6c. Pristine $MoSe_2$ has a negligible value of H_2 evolution, which is in accordance with the previous reports [50,51]. In addition, the 5F-CN and 5N-CN samples demonstrate H_2 evolution rates of 114.5 and 136.8 μmol g^{-1} h^{-1}, respectively, which are higher than other F-CN and N-CN samples. Furthermore, the achieved photocatalytic hydrogen evolution rates of $MoSe_2$/g-C_3N_4 are essentially comparable to a number of recent g-C_3N_4-based photocatalysts reports (Table S1) [24,26,61,62]. The rates of H_2 evolution decrease with higher amounts of $MoSe_2$ (*i.e.* 7 and 10 wt%), which can be attributed to the shielding effect of the light absorption caused by excessive $MoSe_2$ nanostructures [25,31]. It is worth mentioning that all the N-CN samples exemplify slightly higher photocatalytic H_2 evolution rates than the F-CN samples (Fig. 6c), which stemmed from their diverse structures and morphologies. In this instant, the coherent sheet-on-sheet heterointerfaces of N-CN play a decisive role over F-CN in the H_2 evolution as a result of favorable charge transfer and separation in N-CN by benefitting from the advantages of face-to-face interaction and large contact interface area. Hence, geometry and morphological engineering of desired nanoarchitectures are of paramount significance in the photocatalytic applications. In order to examine the stability of photocatalysts, the recycling test was performed by utilizing the optimal 5F-CN and 5N-CN samples (Fig. 6d). No obvious decrease in the H_2 evolution rate is detected after four successive runs of photocatalytic reaction, signifying the high stability and durability of these two typical types of $MoSe_2$/g-C_3N_4 hybrid photocatalysts. It is noteworthy that the structure and morphology of the spent 5F-CN and 5N-CN samples basically keep unchanged as attested by the TEM and XRD analyses (Fig. S7–S9), highlighting that the as-prepared $MoSe_2$/g-C_3N_4 photocatalysts are highly stable under prolonged photocatalytic H_2 reaction.

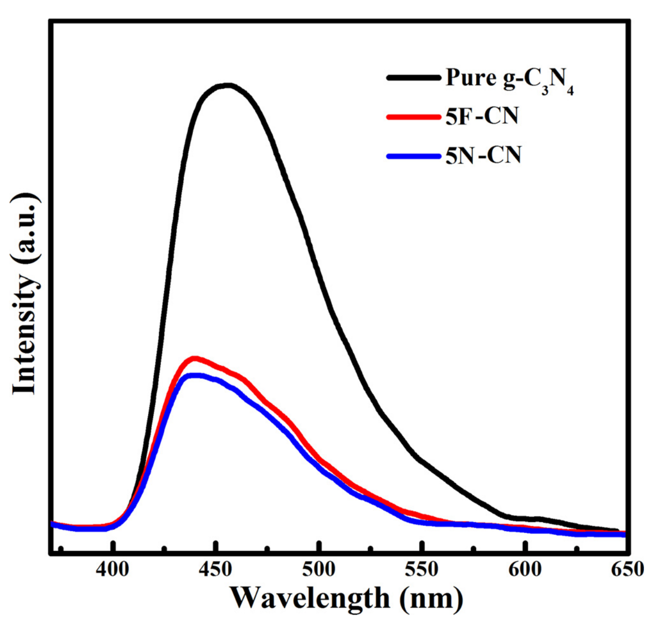

Fig. 7. PL spectra of pure g-C_3N_4, 5F-CN and 5N-CN samples.

To gain further evidence on the interfacial charge transfer phenomenon, the steady-state PL spectroscopy of the $MoSe_2$/g-C_3N_4 hybrid systems was examined in comparison with that of pure g-C_3N_4 (Fig. 7). Pure g-C_3N_4 exhibits a strong emission peak at approximately 455 nm, in which its high intensity accounts for the high recombination rate of photogenerated electron-hole pairs. Nevertheless, the PL intensities remarkably drop when coupling 5 wt% of $MoSe_2$ nanostructures with g-C_3N_4 nanosheets, evincing that the recombination of charge carriers in g-C_3N_4 is prominently retarded by the effective interfacial charge transfer between g-C_3N_4 and $MoSe_2$ nanostructures. What is of even interest is that the PL intensity of 5N-CN is lower than that of 5F-CN, revealing its lower recombination rate of electron-hole pairs owing to the distinctive sheet-on-sheet attributes in the 5N-CN hybrid system. Furthermore, the interfacial charge transfer can be illustrated by the decreased PL lifetime (Fig. S10). The average emission lifetime of pure g-C_3N_4 is 3.24 ns, whereas 5F-CN and 5N-CN exhibit lifetimes of 1.13 ns and 0.33 ns, respectively. The significantly decreased PL lifetime can be assigned to the rapid charge transfer in $MoSe_2$ loaded g-C_3N_4, which reduces the recombination of photo-excited electron-hole pairs [21,25,31]. Moreover, the lifetime of 5N-CN is shorter than that of 5F-CN, signifying that the network-like $MoSe_2$ nanostructure demonstrates more efficient charge transfer and separation compared to the flower-like $MoSe_2$. This is consistent with the obtained photocatalytic hydrogen evolution rate.

Photoelectrochemical (PEC) measurement was performed to delve

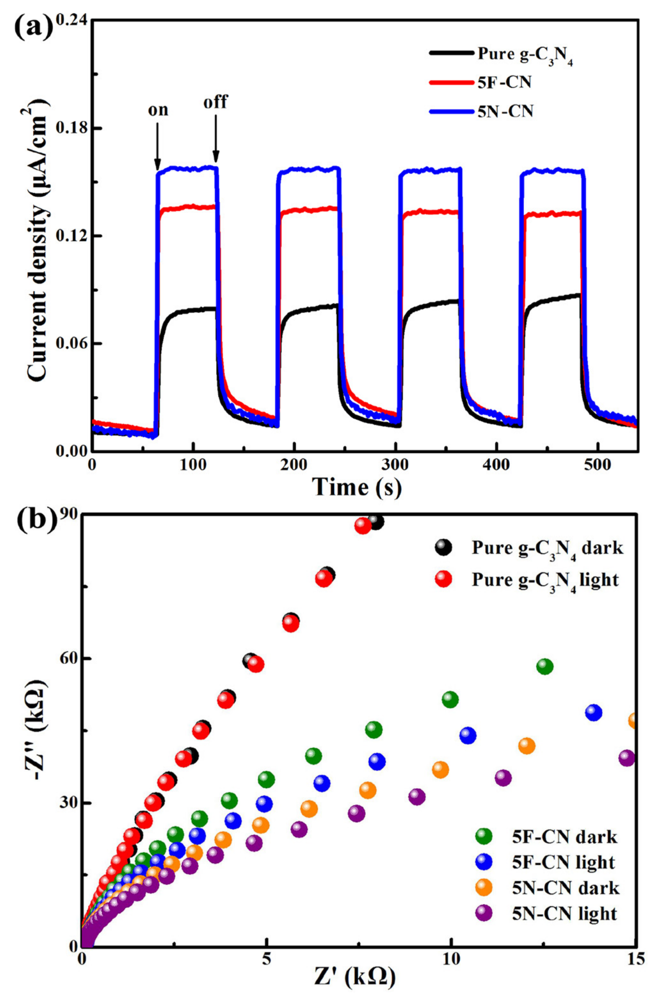

Fig. 8. Transient photocurrent response curves (a) and EIS Nyquist plots (b) of pure g-C_3N_4, 5F-CN and 5N-CN samples.

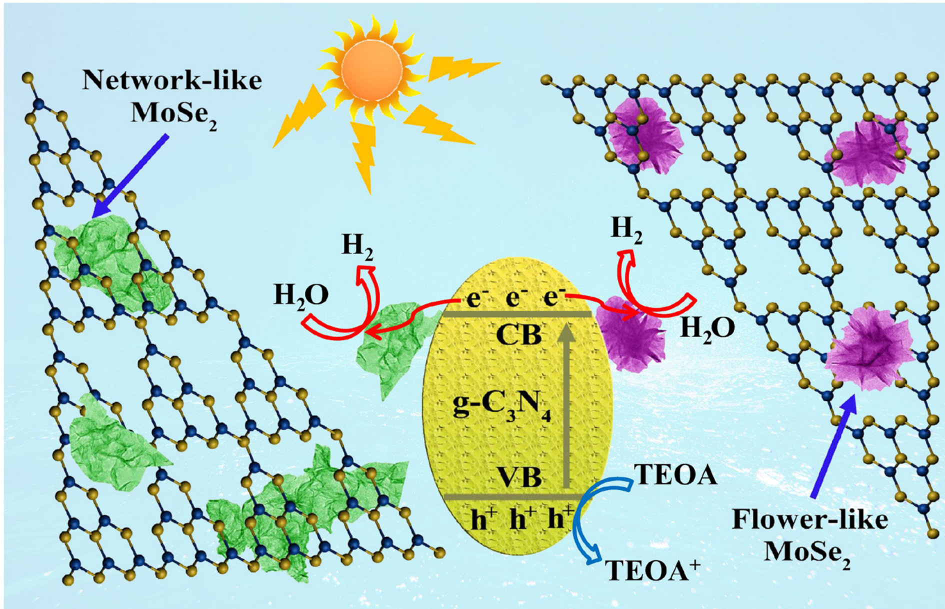

Fig. 9. Schematic of photocatalytic H_2 evolution for the $MoSe_2$/g-C_3N_4 hybrid systems by incorporating with flower-like and network-like $MoSe_2$.

into investigating the separation efficiency of the photoinduced electron-hole pairs in the photoelectrodes. As divulged in Fig. 8a, all the electrodes show good reproducibility of photocurrent, inferring that the samples are stable and that the photoresponses are reversible under the light on-off cycle. The photocurrent density of 5F-CN and 5N-CN is much stronger than that of pure g-C_3N_4, indicating that the g-C_3N_4-based hybrid system demonstrates a higher separation rate of photogenerated electron-hole pairs after incorporating with $MoSe_2$ nanostructures [21,25,31]. Furthermore, the 5N-CN sample exhibits higher photocurrent density than 5F-CN, thus underpinning its higher charger carrier transfer, migration and separation rate. Fig. 8b manifests the EIS Nyquist plots of pure g-C_3N_4, 5F-CN and 5N-CN electrodes. Apparently, the arc radii of the Nyquist plots for the two $MoSe_2$/g-C_3N_4 electrodes are eminently smaller compared to that for pure g-C_3N_4 in the dark and under visible light irradiation owing to the loading of $MoSe_2$. This implied that the separation and transfer efficiency of photogenerated electron-hole pairs were greatly increased by means of an intimate interfacial interaction between g-C_3N_4 and $MoSe_2$. By comparing both morphologically-controlled $MoSe_2$/g-C_3N_4 samples, 5N-CN possesses the smallest arc radius of the Nyquist plot, which explicates the most effective interfacial electron transfer at the intimate sheet-on-sheet heterointerface between g-C_3N_4 and network-like $MoSe_2$, thus contributing to the overall improvement of photocatalytic activity [63–65]. Overall, the PEC results concur very well with our aforementioned photocatalytic H_2 evolution activity (Fig. 6) and PL analysis (Fig. 7).

Based on the above results, the mechanism of photocatalytic H_2 production in the $MoSe_2$/g-C_3N_4 hybrid systems was shown in Fig. 9. When the $MoSe_2$/g-C_3N_4 heterostructure is illuminated by visible light, the electrons at the valence band (VB) of g-C_3N_4 are excited to the conduction band (CB), leaving holes in the VB which are quenched by TEOA. The photoexcited electrons rapidly transfer to the metallic $MoSe_2$ nanostructures *via* the intimate interfaces between g-C_3N_4 nanosheets and $MoSe_2$. Without the presence of noble metals, the migrated electrons can directly react with protons in water to produce molecular H_2 through $MoSe_2$ nanostructures, which have abundant exposed active sites. Furthermore, the g-C_3N_4-based hybrid systems coupled with network-like $MoSe_2$ nanostructures have a higher BET surface area and total pore volume than the flower-like $MoSe_2$ as surmised by the BET analysis (Fig. 3). Therefore, in light of the ample active catalytic sites of $MoSe_2$ and the exceptional sheet-on-sheet heterojunction interfaces between g-C_3N_4 and network-like $MoSe_2$, such fascinating features are indeed beneficial for the light absorption, large contact areas with water, and boosted separation of the charge carriers due to the face-to-face interaction, leading to the higher photocatalytic H_2 evolution rate in N-CN [43,66].

4. Conclusions

In summary, flower-like and network-like $MoSe_2$ nanostructures were coupled with porous g-C_3N_4 nanosheets through a simple solution-phase method. These two different morphological designs of $MoSe_2$/g-C_3N_4 hybrid photocatalysts unveiled efficient H_2 evolution activity without any noble metals under visible light. The optimal loading of flower-like and network-like $MoSe_2$ nanostructures in the g-C_3N_4-based hybrid systems was determined to be 5 wt%, giving maximum H_2 evolution rates of 114.5 μmol $h^{-1}g^{-1}$ and 136.8 μmol $h^{-1}g^{-1}$, respectively. Interestingly, the network-like $MoSe_2$ nanostructures decorated with g-C_3N_4 demonstrated more excellent photocatalytic H_2 generation compared to the flower-like $MoSe_2$. This phenomenon was attributed to the highly effective charge migration and separation on the basis of the synergistic effect arising from the unique sheet-on-sheet heterointerface in N-CN, which was in concord with the BET, steady-state PL and PEC analyses. As such, it is envisioned that this research opens up a new window and paradigm for the hybridization of layered nanostructures and colloidally synthesized transition metal selenides for a plethora of multifunctional applications in energy storage and solar energy conversion.

Acknowledgements

This work was partially supported by the National Natural Science Foundation of China (Grant Nos. 51471137 and 51371154) and the National Key R&D Program of China (Grant No. 2016YFA0202602). W.-J. Ong is thankful for the support from the IMRE, A*STAR in Singapore.

Appendix A. Supplementary data

Supplementary material related to this article can be found, in the online version, at doi:https://doi.org/10.1016/j.apcatb.2018.03.102.

References

[1] T. Hisatomi, J. Kubota, K. Domen, Chem. Soc. Rev. 43 (2014) 7520–7535.
[2] W.-J. Ong, L.L. Tan, Y.H. Ng, S.T. Yong, S.P. Chai, Chem. Rev. 116 (2016) 7159–7329.
[3] D. Masih, Y. Ma, S. Rohani, Appl. Catal. B Environ. 206 (2017) 556–588.
[4] G.G. Zhang, Z.-A. Lan, L.H. Lin, S. Lin, X.C. Wang, Chem. Sci. 7 (2016) 3062–3066.
[5] W.-J. Ong, Front. Mater. 4 (2017) 11, http://dx.doi.org/10.3389/fmats.2017.00011.
[6] S. Cao, J. Yu, J. Phys. Chem. Lett. 5 (2014) 2101–2107.
[7] L. Zhou, H. Zhang, H. Sun, S. Liu, M.O. Tade, S. Wang, W. Jin, Catal. Sci. Technol. 6 (2016) 7002–7023.
[8] L. Jiang, X. Yuan, Y. Pan, J. Liang, G. Zeng, Z. Wu, H. Wang, Appl. Catal. B Environ. 217 (2017) 388–406.
[9] M. Zhang, X. Wang, Energy Environ. Sci. 7 (2014) 1902–1906.
[10] S. Yang, Y. Gong, J. Zhang, L. Zhan, L. Ma, Z. Fang, R. Vajtai, X. Wang, P.M. Ajayan, Adv. Mater. 25 (2013) 2452–2456.
[11] Y. Zheng, J. Liu, J. Liang, M. Jaroniec, S.Z. Qiao, Energy Environ. Sci. 5 (2012) 6717–6731.
[12] Y. Wang, X.C. Wang, M. Antonietti, Angew. Chem. Int. Ed. 51 (2012) 68–89.
[13] Y.F. Zhao, Z.Y. Yang, Y.X. Zhang, L. Jing, X. Guo, Z.T. Ke, P.W. Hu, G.X. Wang, Y.M. Yan, K.N. Sun, J. Phys. Chem. C 118 (2014) 14238–14245.
[14] J. Wen, J. Xie, X. Chen, X. Li, Appl. Surf. Sci. 391 (Part B) (2017) 72–123.
[15] Y. Hou, A.B. Laursen, J. Zhang, G. Zhang, Y. Zhu, X. Wang, S. Dahl, I. Chorkendorff, Angew. Chem. Int. Ed. 52 (2013) 3621–3625.
[16] H. Zhao, Y. Dong, P. Jiang, H. Miao, G. Wang, J. Zhang, J. Mater. Chem. A 3 (2015) 7375–7381.
[17] M.S. Akple, J. Low, S. Wageh, A.A. Al-Ghamdi, J. Yu, J. Zhang, Appl. Surf. Sci. 358 (Part A) (2015) 196–203.
[18] J. Hong, Y. Wang, Y. Wang, W. Zhang, R. Xu, ChemSusChem 6 (2013) 2263–2268.
[19] Z.H. Chen, P. Sun, B. Fang, Z.G. Zhang, X.M. Fang, J. Phys. Chem. C 118 (2014) 7801–7807.
[20] Y. Hou, Y. Zhu, Y. Xu, X. Wang, Appl. Catal. B Environ. 156 (2014) 122–127.
[21] A. Indra, A. Acharjya, P.W. Menezes, C. Merschjann, D. Hollmann, M. Schwarze, M. Aktas, A. Friedrich, S. Lochbrunner, A. Thomas, M. Driess, Angew. Chem. 129 (2017) 1675–1679.
[22] D. Zeng, W. Xu, W.-J. Ong, J. Xu, H. Ren, Y. Chen, H. Zheng, D.-L. Peng, Appl. Catal. B Environ. 221 (2018) 47–55.
[23] H. Zhao, S. Sun, P. Jiang, Z.J. Xu, Chem. Eng. J. 315 (2017) 296–303.
[24] P. Ye, X. Liu, J. Locozzia, Y. Yuan, L. Gu, G. Xu, Z. Lin, J. Mater. Chem. A 5 (2017) 8493–8498.
[25] D. Zeng, W.-J. Ong, H. Zheng, M. Wu, Y. Chen, D.-L. Peng, M.-Y. Han, J. Mater. Chem. A 5 (2017) 16171–16178.
[26] J. Wen, J. Xie, R. Shen, X. Li, X.Y. Luo, H. Zhang, A. Zhang, G. Bi, Dalton Trans. 46 (2017) 1794–1802.
[27] L. Bi, X. Gao, L. Zhang, D. Wang, X. Zou, T. Xie, ChemSusChem 11 (2018) 276–284.
[28] Z. Qin, Y. Chen, Z. Huang, J. Su, L. Guo, J. Mater. Chem. A 5 (2017) 19025–19035.
[29] H. Zhao, J. Wang, Y. Dong, P. Jiang, ACS Sustainable Chem. Eng. 5 (2017) 8053–8060.
[30] S.-S. Yi, J.-M. Yan, B.-R. Wulan, S.-J. Li, K.-H. Liu, Q. Jiang, Appl. Catal. B Environ. 200 (2017) 477–483.
[31] C. Li, Y. Du, D. Wang, S. Yin, W. Tu, Z. Chen, M. Kraft, G. Chen, R. Xu, Adv. Funct. Mater. 27 (2017) 1604328.
[32] H. Zhao, P. Jiang, W. Cai, Chem. Asian J. 12 (2017) 361–365.
[33] Y. Yu, S.-Y. Huang, Y. Li, S.N. Steinmann, W. Yang, L. Cao, Nano Lett. 14 (2014) 553–558.
[34] L. Ma, Y. Hu, G. Zhu, R. Chen, T. Chen, H. Lu, Y. Wang, J. Liang, H. Liu, C. Yan, Z. Tie, Z. Jin, J. Liu, Chem. Mater. 28 (2016) 5733–5742.
[35] L. Liao, S. Wang, J. Xiao, X. Bian, Y. Zhang, M.D. Scanlon, X. Hu, Y. Tang, B. Liu, H.H. Girault, Energy Environ. Sci. 7 (2014) 387–392.
[36] D. Geng, X. Zhao, Z. Chen, W. Sun, W. Fu, J. Chen, W. Liu, W. Zhou, K.P. Loh, Adv. Mater. 29 (2017) 1700072.
[37] Z. Gholamvand, D. McAteer, C. Backes, N. McEvoy, A. Harvey, N.C. Berner, D. Hanlon, C. Bradley, I. Godwin, A. Rovetta, M.E.G. Lyons, G.S. Duesberg, J.N. Coleman, Nanoscale 8 (2016) 5737–5749.
[38] S. Mao, Z. Wen, S. Ci, X. Guo, K.K. Ostrikov, J. Chen, Small 11 (2015) 414–419.
[39] Z. Liu, N. Li, H. Zhao, Y. Du, J. Mater. Chem. A 3 (2015) 19706–19710.
[40] W. Guo, Y. Chen, L. Wang, J. Xu, D. Zeng, D.-L. Peng, Electrochim. Acta 231 (2017) 69–76.
[41] Q. Xiang, J. Yu, M. Jaroniec, J. Am. Chem. Soc. 134 (2012) 6575–6578.
[42] Y. Zhu, Q. Ling, Y. Liu, H. Wang, Y. Zhu, Phys. Chem. Chem. Phys. 17 (2015) 933–940.
[43] J. He, L. Chen, F. Wang, Y. Liu, P. Chen, C.T. Au, S. Yin, ChemSusChem 9 (2016) 624–630.
[44] G. Chen, N. Ding, F. Li, Y. Fan, Y. Luo, D. Li, Q. Meng, Appl. Catal. B Environ. 160 (2014) 614–620.
[45] S. Zhang, H. Yang, H. Gao, R. Cao, J. Huang, X. Xu, ACS Appl. Mater. Interfaces 9 (2017) 23635–23646.
[46] K. Pramoda, U. Gupta, M. Chhetri, A. Bandyopadhyay, S.K. Pati, C.N.R. Rao, ACS Appl. Mater. Interfaces 9 (2017) 10664–10672.
[47] J. Sun, L. Duan, Q. Wu, W. Yao, Chem. Eng. J. 332 (2018) 449–455.
[48] Y. Huang, Y.E. Miao, J. Fu, S. Mo, C. Wei, T. Liu, J. Mater. Chem. A 3 (2015) 16263–16271.
[49] C. Xu, S.J. Peng, C.L. Tan, H.X. Ang, H.T. Tan, H. Zhang, Q.Y. Yan, J. Mater. Chem. A 2 (2014) 5597–5601.
[50] M.-Q. Yang, Y.-J. Xu, W. Lu, K. Zeng, H. Zhu, Q.-H. Xu, G.W. Ho, Nat. Commun. 8 (2017) 14224.
[51] D. Zeng, L. Xiao, W.J. Ong, P. Wu, H. Zheng, Y. Chen, D.-L. Peng, ChemSusChem 10 (2017) 4624–4631.
[52] Y. Li, W. Shen, Chem. Soc. Rev. 43 (2014) 1543–1574.
[53] X. Huang, Z. Zeng, H. Zhang, Chem. Soc. Rev. 42 (2013) 1934–1946.
[54] Y. Pan, Y.R. Liu, J.C. Zhao, K. Yang, J.L. Liang, D.D. Liu, W.H. Hu, D.P. Liu, Y.Q. Liu, C.G. Liu, J. Mater. Chem. A 3 (2015) 1656–1665.
[55] R. Bera, S. Kundu, A. Patra, ACS Appl. Mater. Interfaces 7 (2015) 13251–13259.
[56] W.-J. Ong, L.K. Putri, Y.-C. Tan, L.L. Tan, N. Li, Y.H. Ng, X. Wen, S.P. Chai, Nano Res. 10 (2017) 1673–1696.
[57] M.K. Bhunia, K. Yamauchi, K. Takanabe, Angew. Chem. Int. Ed. 126 (2014) 11181–11185.
[58] Y. Cui, Z. Ding, P. Liu, M. Antonietti, X. Fu, X. Wang, Phys. Chem. Chem. Phys. 14 (2012) 1455–1462.
[59] S. Zhou, Y. Liu, J. Li, Y. Wang, G. Jiang, Z. Zhao, D. Wang, A. Duan, J. Liu, Y. Wei, Appl. Catal. B Environ. 158 (2014) 20–29.
[60] S. Samanta, S. Martha, K. Parida, ChemCatChem 6 (2014) 1453–1462.
[61] J. Yu, S. Wang, B. Cheng, Z. Lin, F. Huang, Catal. Sci. Technol. 3 (2013) 1782–1789.
[62] D. Zeng, W.J. Ong, Y. Chen, S.Y. Tee, C.S. Chua, D.-L. Peng, M.-Y. Han, Part. Part. Syst. Charact. 35 (2018) 1700251.
[63] Y. Sun, Z. Sun, S. Gao, H. Cheng, Q. Liu, F. Lei, S. Wei, Y. Xie, Adv. Energy Mater. 4 (2014) 1300611.
[64] M.-Q. Yang, C. Han, Y.-J. Xu, J. Phys. Chem. C 119 (2015) 27234–27246.
[65] L. Shang, B. Tong, H. Yu, G.I.N. Waterhouse, C. Zhou, Y. Zhao, M. Tahir, L.-Z. Wu, C.-H. Tung, T. Zhang, Adv. Energy Mater. 6 (2016) 1501241.
[66] J. Low, S. Cao, J. Yu, S. Wageh, Chem. Commun. 50 (2014) 10768–10777.